Arabian Journal for Science and Engineering (2021) 46:4791–4810
https://doi.org/10.1007/s13369-020-05167-1

RESEARCH ARTICLE-CIVIL ENGINEERING

Long-Term Drained and Post-liquefaction Cyclic Behaviour of Offshore Wind Turbine in Silty Sand Using Element Tests

Sangeet Kumar Patra[1] · **Sumanta Haldar**[1]

Received: 4 August 2020 / Accepted: 18 November 2020 / Published online: 4 January 2021

Abstract

Offshore wind turbine (OWT) structure foundations and soil are subjected to long-term cyclic loading from wind and waves. Loads due to earthquake also act on the OWT system in seismically active areas. The long-term dynamic behaviour of the OWT is challenging due to the complex nature of dynamic loads. The soil stiffness changes due to the application of cyclic loading, which leads to a change in the natural frequency and response of the OWT system. Therefore, the assessment of long-term dynamic behaviour soil surrounding the foundation of the OWT structure is essential due to the operational condition and seismic event. In this study, element tests are conducted utilizing cyclic triaxial test apparatus to examine the long-term drained and post-liquefaction long-term cyclic behaviour of silty sand. Secant shear modulus and damping ratio are estimated under drained condition due to 10,000 load cycles. Silty sand behaviour at liquefied phase and post-liquefaction long-term cyclic behaviour phases are investigated at different effective confining pressure, relative density, and shear strain rate. Based on the element tests, a numerical model is proposed predicting the long-term fundamental frequency of OWT to avoid resonance.

Keywords Dynamic soil properties · Liquefaction · Post-liquefaction · Monopile · Offshore wind turbine

1 Introduction

The increase in greenhouse gases due to the burning of fossil fuels is a threat to the environment. The crucial environmental challenge is to reduce the generation of greenhouse gases, which cause global warming. Wind energy is considered a cost-effective and renewable energy source, and monopile is commonly used as a foundation for offshore wind turbines (OWT) due to its simple shape, easy constructional procedure, and cost-effectiveness [1, 2]. Monopile is a long slender structure made up of steel with 30–40 m length, 3.5–6 m outer diameter, and installed at a water depth of 10–25 m [3]. The dynamic loads acting on the OWT structure are due to rotor excitation, wind, wave, ocean current, tower shadowing effect, and wind gusts [4]. During the design life of the OWT structure (i.e. generally 25–30 years), it is subjected to 10^7 to 10^8 cycles of loading [5]. Modern variable speed wind turbines operate at a rotor speed of 10–20 rpm, i.e. excitation frequency interval is about 0.1–0.3 Hz [6]. This rotor frequency is referred to as 1P frequency. The typical frequency ranges of wave acting on the OWT structure is 0.05–0.5 Hz [7, 8]. Wind load acts on the OWT structure at a frequency of 0.01 Hz [9]. Blade passing frequency (i.e. 2P frequency for two-bladed and 3P frequency for three-bladed) also induces dynamic load on the OWT structure due to the tower shadowing effect [10]. Offshore wind turbines are designed as the soft-stiff design approach, where the fundamental frequency of the soil-monopile-tower system is placed between the rotor frequency (1P) and blade passing frequency (3P for three-bladed turbines) [11]. DNVGL-ST-0126 [12] guidelines suggest that the OWT system's fundamental frequency should be at least 10% away from operational 1P and 2P/3P frequencies to avoid resonance.

Wind turbines are constructed in seismic areas due to increasing energy demand. Many countries, such as the USA, China, India, and Southeast Asia, are in highly seismic zones, where magnitude M9-class earthquakes may occur [13]. Many offshore sites consist of loose silty sands and

✉ Sumanta Haldar
sumanta@iitbbs.ac.in

Sangeet Kumar Patra
skp16@iitbbs.ac.in

1 Department of Civil Engineering, School of Infrastructure, Indian Institute of Technology Bhubaneswar, Jatni, Odisha 752050, India

sandy silts, which is susceptible to liquefaction during earthquakes [14]. Many offshore sites consist of loose silty sands and sandy silts. To cite a few, the most common sediment types in the China seas are sand, silt, and silty clay [15]. The soils in Hoogly delta, Mahanadi Basin, north of Godavari delta at Indian offshore are mostly medium dense to dense sand mixed with nominal per cent of silt [14, 16]. Silty sand is also found on the south-western coast of Korea [17].

All these locations have the potential for offshore wind farm developments. The dynamic response of the OWT structure is mostly affected during seismic liquefaction due to strong ground motion. The fundamental frequency of the OWT system approach towards operating frequency momentarily and resonance condition may arise due to the softening of soil during liquefaction. Thereafter, the excess pore water pressure gets released completely, and soil regains its strength. OWT's operational load develops a drained response in the soil as no pore water pressure accumulates during the loading cycle, whereas the soil behaviour around the foundation is undrained in case of seismic loading [11]. During earthquakes, wind turbines also experience wind and wave loads if they are located offshore. Essential aspects of estimating the seismic risk of wind turbines were often not made. For example, no studies consider concurrent wave, wind, and seismic action on offshore wind turbines under drained conditions, liquefaction, and post-liquefaction conditions. This is inadequate, as it is essential to consider all concurrent and subsequent actions when a seismic force acts on a turbine.

Past studies by Lombardi [4], Bhattacharya et al. [18], and Cox and Jones [19] showed that the fundamental frequency of OWT structure changes with cycles of loading as the stiffness of the soil-foundation changes [20]. Abhinav and Saha [21] reported that the change in the fundamental frequency of OWT structure mainly depends on the induced shear strain level in the soil surrounding the monopile, and it also depends on the type of soil surrounding the monopile. Cui et al. [1] showed that the stiffness of granular soil increases under cyclic loading due to the densification effect. Nikitas et al. [9] conducted series of cyclic simple shear tests on the sand and reported that secant shear modulus increases at a high rate during the initial loading cycles, and then it increases at a slower rate. They also reported the effect of relative density, effective confining pressure, and shear strain rate on the secant shear modulus of the sand. Wang et al. [22] performed centrifuge tests to investigate the lateral bearing behaviour of the improved suction bucket foundation (ISBF) on sandy soil and reported that the stiffness and lateral displacement of foundation increase significantly for initial loading cycles and remains constant in the subsequent loading cycles. Based on distinct element method simulation, Duan [23] reported that sand stiffness increases with loading cycles due to the densification effect. Bhattacharya and Adhikari [24], Cuéllar et al. [25], LeBlanc [8] stated that the foundation stiffness for a monopile in sandy soil increases due to the densification of the soil next to the pile. The primary reason for the change in foundation stiffness is due to the soil's strain-hardening behaviour supporting the pile [11]. The API [26] and DNV-GL-ST-0126 [12] suggested the degradation of foundation stiffness under cyclic loading in sandy soil. Based on four years of monitoring data, Weijtens and Deviendt [27] showed that OWT's first natural frequency increases by about 5% in sandy soil. Prediction of the temporal evaluation of OWT's natural frequency is essential as the over and under-prediction of natural frequency could be conservative [28]. OWT is subjected to various loads having a wide frequency band from wind turbulence, wave, and 1P and 3P loads. Hence, it is essential to predict long-term natural frequency to estimate the structure's dynamic amplification factor for the non-liquefied condition, liquefied soil, and post-liquefaction condition. However, less attention has been given in this direction. Furthermore, limited studies are available on the effect of liquefaction on the change in frequency and damping of OWT structures.

The present study focuses on the assessment of the dynamic behaviour of silty sand using cyclic triaxial test equipment. To study the long-term drained cyclic behaviour of silty sand, strain-controlled cyclic triaxial tests were carried out on dry samples with relative densities 30%, 50%, and 70% axial strain amplitude ± 0.2% and ± 0.3% applied for 10,000 cycles. Each sample was tested at 50 kPa, 100 kPa, and 150 kPa confining pressures. To check the long-term cyclic behaviour during the post-liquefaction stage, first, the saturated samples having relative densities 30%, 50% were liquefied at pre-determined cyclic stress ratio by performing the stress-controlled cyclic triaxial test on the soil samples. Each sample was tested at 50 kPa effective confining pressure. The excess pore water pressure is allowed to release completely, and strain-controlled drained cyclic triaxial test with axial strain amplitude ± 0.2% were carried out to 10,000 load cycles liquefied soil sample to check the dynamic response of silty sand in the post-liquefaction stage. Finally, a numerical model is developed using a nonlinear beam of the Winkler model to predict OWT's long-term fundamental frequency due to operational loading and concurrent wave, wind, and seismic action. This could ensure the avoidance of resonance to minimize fatigue damage.

2 Experimental Programs

2.1 Testing Device and Sample Preparation

To examine the effect of liquefaction on the dynamic response of the OWT structure, the liquefaction-susceptible silty sand is collected from nearshore locations of Odisha, India, as a representative soil sample in this study. To study the long-term cyclic behaviour of silty sand, strain-controlled cyclic triaxial tests were carried out on dry samples of silty sand using cyclic triaxial testing equipment. Figure 1 shows the cyclic triaxial equipment setup and its components. The loading system consists of a load frame with a load-carrying capacity 50 kN and a pneumatic actuator capable of performing strain-controlled and stress-controlled tests with frequency range 0.1 Hz to 2 Hz. The different sensor includes servo-controlled submersible load cell with a capacity of measuring load up to 5 kN, an LVDT capable of measuring ± 50 mm axial displacement, and three transducers capable of measuring 1000 kPa chamber pressure, back pressure and pore water pressure are used in the present study.

Dry specimens of silty sand having size 50 mm diameter and 100 mm height with relative densities 30%, 50%, and 70% are prepared by employing the dry-pluviation technique. The soil's dry densities are 1.47 g/cc, 1.52 g/cc and 1.58 g/cc for 30%, 50%, and 70% relative densities, respectively. A pre-weighed dry sample of silty sand corresponding to the desired relative density is poured inside the membrane-lined split mould through a funnel with a tube attached to the spout. The tube was placed at the bottom of the membrane-lined split mould. The tube was slowly raised along the axis of symmetry, and the mould was filled with soil in five layers, and each layer is compacted with a tamping rod to achieve the desired density. Figure 2 shows the grain size distribution curve of silty sand. The sample contains 90% sand, mostly fine graded with 9.7% silt and 0.3% clay. The soil is classified as silty sand (SM) as per the unified soil classification system. The grain size distribution of liquefiable soil ranges specified by the Japanese Seismic Code for Port Structures [29, 30] is superimposed. According to these ranges, the silty sand's grain size distribution falls in the highly susceptible liquefaction zone. The physical properties of silty sand are listed in Table 1.

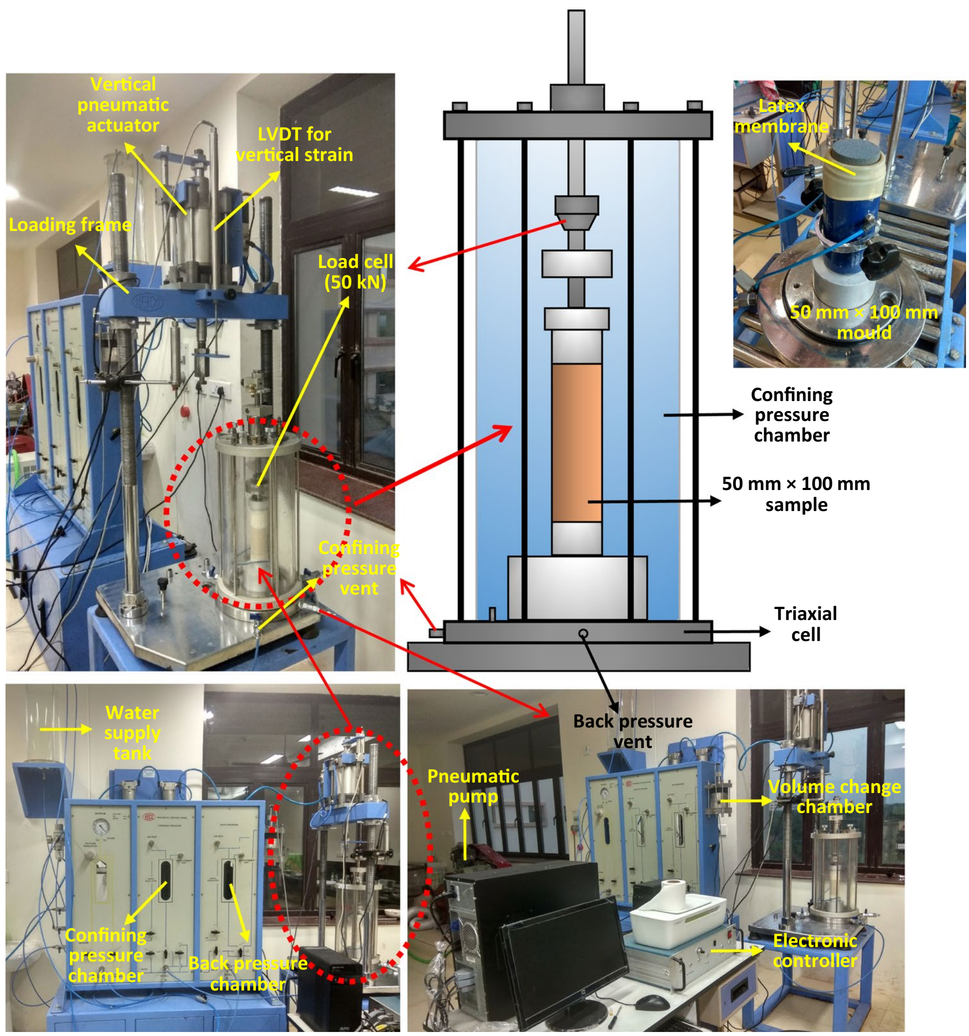

Fig. 1 Cyclic triaxial equipment setup and its components

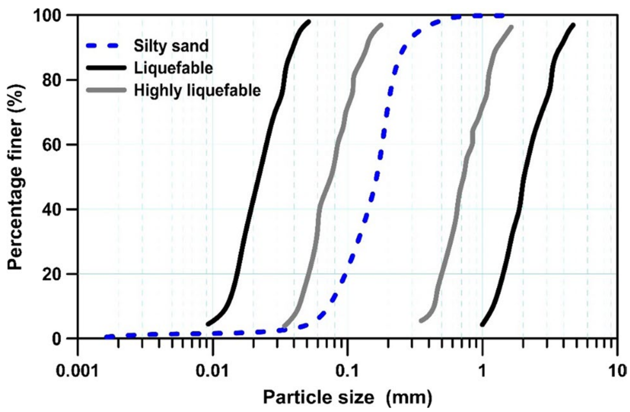

Fig. 2 The grain size distribution of silty sand considered in this study and grain size distributions of liquefaction-prone sands

Table 1 Properties of silty sand

Parameter	Value	Reference standard
Specific gravity, G	2.6	IS 2720: Part 3 (1980) [31]
Maximum void ratio, e_{max}	0.85	IS 2720: Part 14 (2006) [32]
Minimum void ratio, e_{min}	0.56	IS 2720: Part 14 (2006) [32]
Uniformity coefficient, C_u	2.8	–
Sand (%)	89	–
Silt (%)	9.7	–
Clay (%)	0.3	–

2.2 Long-term Cyclic Drained Tests

The operational load acting on the OWT structure generates a drained response in the soil as no pore water pressure accumulation during the loading cycles in sandy soil. As a result, the use of dry sand for OWT's operational condition seems to be justified [11]. Hence, in the present study, the long-term dynamic behaviour of silty sand due to the operational load acting on the OWT structure is studied by performing a series of strain-controlled cyclic triaxial tests. The strain-controlled tests were carried out on dry specimens of silty sand having initial relative densities 30%, 50%, and 70% with axial strain amplitude ± 0.2% and ± 0.3% applied at 0.5 Hz frequency for 10,000 cycles. Each sample was tested at 50 kPa, 100 kPa, and 150 kPa confining pressures. It is observed that the frequency of cyclic loading has no significant influence on the dynamic soil properties of sand (e.g. [33–36]). Hence, all samples were tested at 0.5 Hz loading frequency.

2.3 Cyclic Undrained and Post-Liquefaction Long-Term Cyclic Drained Tests

Offshore wind turbines embedded in silty sand may liquefy due to strong seismic motion, which may affect the dynamic response of the OWT structure. The excess pore water pressure generated during the liquefaction stage decreases gradually soon after the strong seismic motion. Therefore, the assessment of the dynamic behaviour of soil during the post-liquefaction stage under the operational loading condition is essential. As the loading is only operational load, the post-liquefaction behaviour of the silty sand is drained in nature.

To examine the long-term cyclic behaviour of silty sand during the post-liquefaction stage, the samples are first subjected to liquefaction by performing the stress-controlled undrained cyclic triaxial test at a pre-determined cyclic stress ratio (CSR) of 0.1 and 0.2. The dry samples with initial relative densities 30% and 50% were prepared based on the earlier method. The confining pressure and backwater pressure were then applied at a constant incremental rate to attain the required degree of saturation. The saturation of the specimens was checked by measuring Skempton's pore pressure parameter (B). The specimens were accepted as fully saturated when the Skempton's B parameter reached greater than 0.95. Due to strong seismic motion, usually, 10–15 m of soil below the mudline level liquefies. The average effective lateral stress is found to be 50 kPa, and the relative density varies between 30 and 50% at 10–15 m depth below the mudline level in general (Gulathi [16]). Therefore, each sample was tested by maintaining effective confining pressure (i.e. the difference between confining pressure and backwater pressure) as 50 kPa. The cyclically applied load is stopped when the excess pore water pressure ratio is reached close to 1.0, and thereafter the drainage valve is opened to release the excess pore water pressure. When the excess pore water pressure is released completely, strain-controlled drained cyclic triaxial tests at an axial strain amplitude ± 0.2% is carried out at 0.5 Hz frequency for 10,000 cycles to study the dynamic behaviour of silty sand at the post-liquefaction stage. Table 2 shows the details of the experimental programme.

2.4 Evaluation of Dynamic Soil Parameters

In order to remove unwanted noise and outliers from the recorded data, the Savitzky-Golay smoothing filtering technique [37, 38] is used. The post-processing is done using a *'sgolayfilt'* function in MATLAB. The processed data are used to evaluate the dynamic soil parameters. The hysteresis loop (i.e. the plot of shear stress versus shear strain) is obtained for different cycles of loading and variation of secant shear modulus ($G_{S,N}$) and damping ratio (ξ) of soil with the cycle is estimated for both strain-controlled and stress-controlled cyclic triaxial tests. The inclination of the hysteresis loop depends on the stiffness of the soil, and the tangent shear modulus can describe any point on the loop. The tangent shear modulus varies throughout the cycle of loading. The average value of the tangent shear modulus

Table 2 Experimental program for element testing

Test type	Shear strain amplitude		Relative density (%)	Confining pressure
Strain-controlled drained cyclic triaxial test on dry sand	0.3%		30	50 kPa, 100 kPa, and 150 kPa
			50	
			70	
	0.4%		30	
			50	
			70	
Stress-controlled undrained cyclic triaxial test for liquefaction simulation	CSR	0.1	30	50 kPa
			50	
		0.2	30	
			50	
Strain-controlled cyclic triaxial test at post-liquefaction phase at CSR = 0.1 and 0.2	0.3%		30	50 kPa

over the entire loop (i.e. during one loading cycle) can be approximated as a secant shear modulus [39]. The secant shear modulus (G_S) can be defined as follows:

$$G_S = \frac{\sum_{i=1}^{N} \mathrm{d}y_i \big/ \mathrm{d}x_i}{N-1} \tag{1}$$

where $\mathrm{d}y_i \big/ \mathrm{d}x_i$ is the tangent shear modulus at different points in the hysteresis loop (cf. Fig. 3). N is the total number of points in the hysteresis loop for a particular loading cycle. 199 number of points for each loading cycle was recorded from the automatic data acquisition system attached to the cyclic triaxial testing equipment.

The energy dissipated during one loading cycle can be related to the damping ratio (ξ). The damping ratio can be expressed as the ratio of energy dissipated (W_D) to the maximum strain energy stored (W_S) during one loading cycle [39]. The damping ratio can be expressed as follows:

$$\xi = \frac{1}{4\pi}\frac{W_D}{W_S} = \frac{1}{2\pi}\frac{A_{\mathrm{loop}}}{G_s\gamma_c^2} \tag{2}$$

where A_{loop} is the area of the hysteresis loop G_s is the secant shear modulus and γ_c is the max shear strain amplitude during one loading cycle and can be obtained from the hysteresis loop shown in Fig. 2.

During the strain-controlled cyclic triaxial test, the sample is strained by application of cyclic axial strain (ε) having an amplitude ± 0.2% and ± 0.3%. The corresponding shear strain (γ) is computed using the following equation, (Kokusho [35]):

$$\gamma = (1+\mu)\varepsilon \tag{3}$$

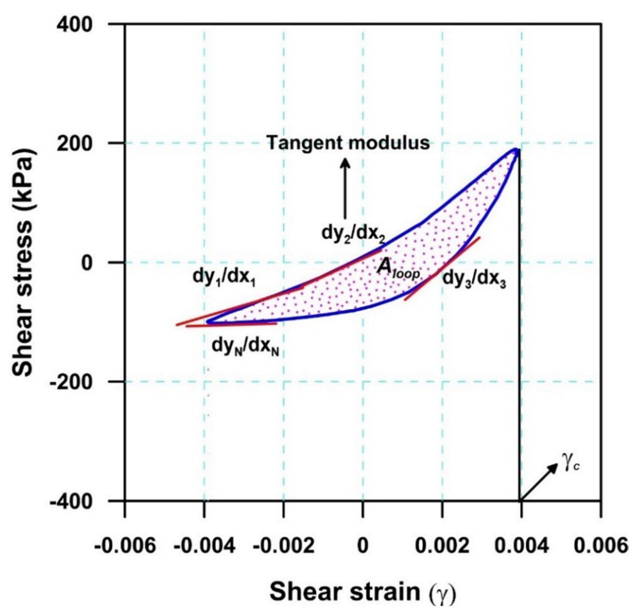

Fig. 3 Hysteresis loop and its various components

where μ is the Poisson's ratio of soil and taken as 0.4 and 0.5 for dry sand and saturated sand in the present study ([40, 41]).

3 Results and Discussion

3.1 Long-term Drained Behaviour of Silty Sand

The hysteresis loops (i.e. the variation of shear stress with shear strain) were obtained from the strain-controlled cyclic triaxial test on dry silty sand are shown in Fig. 4 for initial relative density (D_R) of 50% and at 50 kPa confining pressure. Figure 4a and b shows the variation of shear stress with the shear strain for first, 1000, 2000, 3000, 4000, 5000, 6000, 7000, 8000, 9000, and 10,000 strain cycles (N). From the figure, the stiffening of the hysteresis loop is observed up to 5000 cycles (cf. Fig. 4a) and becomes constant for the subsequent cycles (cf. Fig. 4b). This means that the soil stiffness improves due to the externally applied load thereafter remains constant at a particular strain amplitude. The secant shear modulus and damping ratio are obtained from the hysteresis loop at different cycles as given in Eq. (1)–(3). The effect of confining pressure, relative density, and shear strain rate on the secant shear modulus (G_S) and damping ratio (ξ) of silty sand under drained loading is described in the following sections.

3.1.1 Effect of Confining Pressure

Figure 5a–f summarizes the variation of secant shear modulus ($G_{S,N}$) with loading cycles for 30%, 50% and 70% relative densities at 50 kPa, 100 kPa, and 150 kPa confining pressures at 0.3% and 0.4% of shear strain rate. Similarly, Fig. 6a–f summarizes the variation of damping ratio (ξ) with loading cycles for 30%, 50% and 70% relative densities at 50 kPa, and 150 kPa confining pressures at 0.3% and 0.4% of shear strain rate. From Fig. 5 and Fig. 6, it is observed that secant shear modulus increases and damping ratio decreases up to 5000 load cycles and remains almost constant from 5000 to 10,000 load cycles. It is also observed that secant shear modulus increases, and damping ratio decrease with an increase in confining pressure for a specific value of relative density and shear strain rate.

For example, the secant shear modulus is found to be 41,068 kPa, 51,334 kPa and 62,914 kPa at the end of first cycle for confining pressures (σ_c) = 50 kPa, 100 kPa and 150 kPa, respectively, for relative density (D_R) = 30%, and shear strain = 0.3% (Fig. 5a). Similarly, the secant shear modulus at the end of the 5000 cycles is found to be 54,891 kPa, 68,614 kPa, and 75,249 kPa, respectively, and at a large number of strain cycles (e.g. at the end of 10,000 load cycle), the secant shear modulus is found to be 56,709 kPa, 71,011 kPa, and 77,910 kPa, respectively, for the same test condition. The damping ratio is observed to be 13.6%, and 10% at the end of first cycle and 5.45%, and 6.94% at the end of 10,000 cycle for σ_c = 50 kPa and 150 kPa, respectively, for D_R = 30%, and shear strain = 0.3% (Fig. 6a). From Fig. 5a–f, it is observed that the secant shear modulus is high at high confining pressure, and the change of secant shear modulus is marginal after 5000 loading cycles, as the soil particles come closer and have a denser state of packing as confining pressure increases. It results in higher stiffness to the applied load and resulting in high secant shear modulus. The damping ratio is found to be decreasing with an increase in confining pressure (Fig. 6). A similar kind of behaviour was also observed by Chung et al. [42]. Towhata [43] indicated that

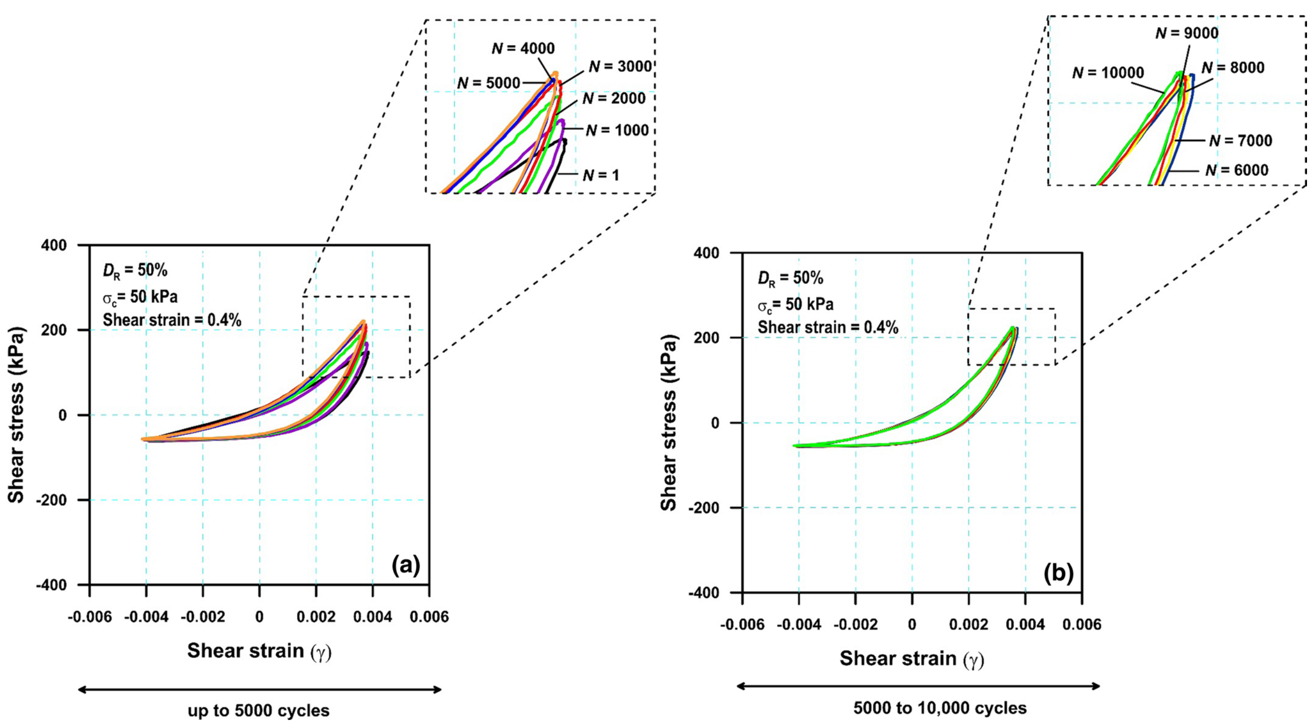

Fig. 4 Hysteresis loop at different cycle of 0.4% shear strain for relative density (D_R) = 50% and confining pressure (σ_c) = 50 kPa **a** up to 5000 cycles **b** 5000 to 10,000 cycles

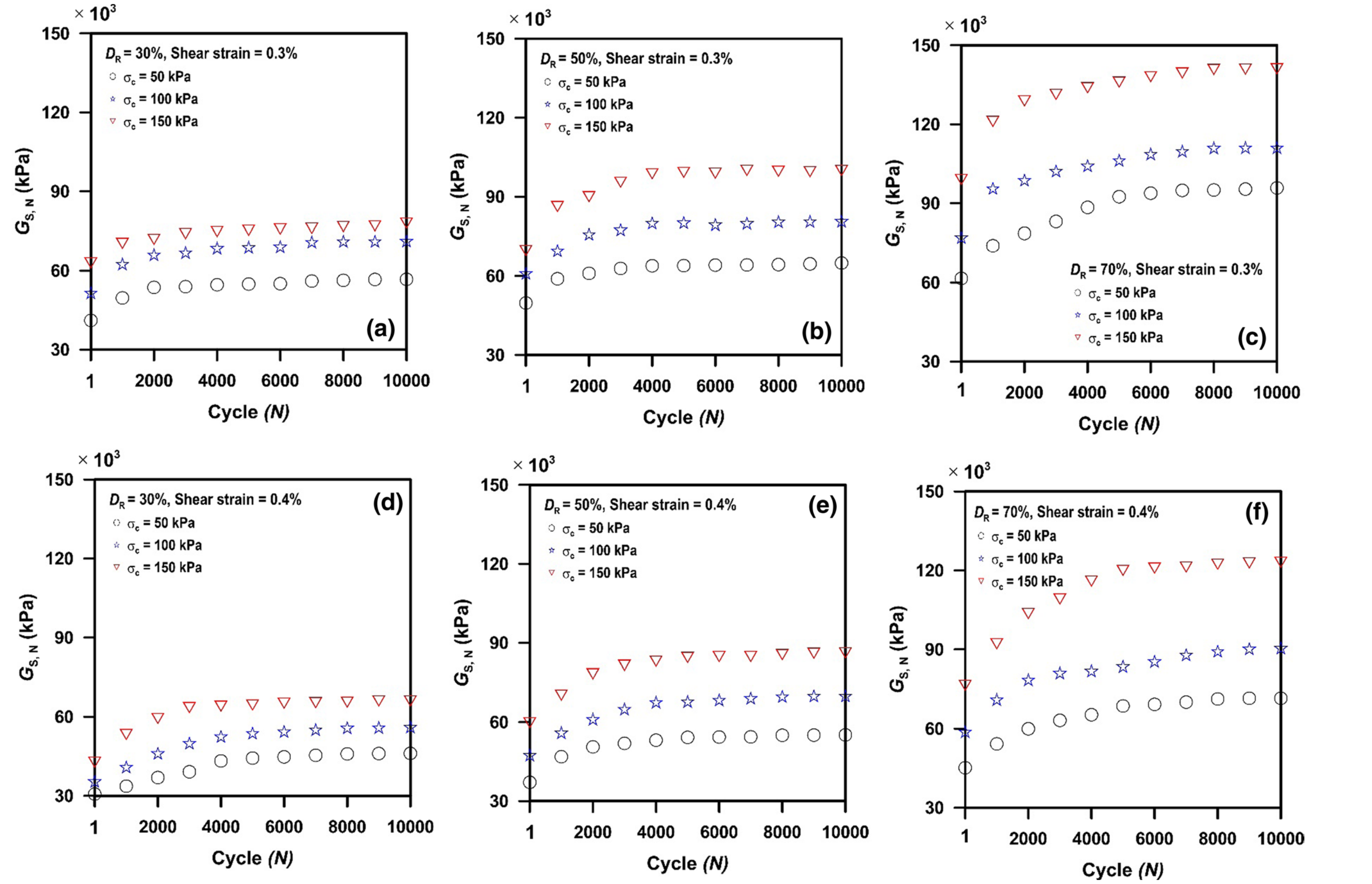

Fig. 5 Variation of shear modulus with cycle for **a** $D_R = 30\%$, **b** $D_R = 50\%$, and **c** $D_R = 70\%$ for shear strain = 0.3% and for **d** $D_R = 30\%$, **e** $D_R = 50\%$, and **f** $D_R = 70\%$ for shear strain = 0.4% at different confining pressures

the magnitude of confining stress in sand affects the nonlinearity. Higher confining stress causes more interaction among soil particles and reduces the discreteness. Thus, the nonlinearity decreases, and damping decreases. The damping ratio is found to be decreasing up to $N = 8000$, which thereafter becomes constant. The denseness of soil increases with an increase in loading cycles, which means the soil particles come closer to each other and show less discreteness. Thus, damping is found to be decreasing with the increasing loading cycle. A similar observation from a cyclic drained test on Toyoura sand is reported in Towhata et al. [44]. A marginal change in damping ratio is observed at 10,000 load cycles regardless of D_R and shear strain. For example, the change in damping ratio is 60% for $\sigma_c = 50$ kPa, whereas the change is only 30% for $\sigma_c = 150$ kPa for $D_R = 30\%$, and shear strain rate = 0.3% at the end of 10,000 cycles (cf. 6 (a)). At higher confining pressure, the soil is already at a dense state and becomes denser and attains the most possible densest state after a certain loading cycle for a particular test condition. Therefore, the change of damping ratio is marginal at the end of the 10,000 loading cycle at higher confining pressure. The marginal change of shear modulus and damping ratio is observed after 5000 load cycles because the soil particle arranges themselves to a most compacted or densest state.

3.1.2 Effect of Relative Density

Figure 7a–f illustrates the variation of secant shear modulus with cycle at 50 kPa, 100 kPa, and 150 kPa effective confining pressures at 0.3% and 0.4% shear strain amplitude and for $D_R = 30\%$, 50% and 70%. Similarly, Fig. 8a–f outlines the variation of damping ratio with the number of strain cycles at 50 kPa, 100 kPa, and 150 kPa confining pressures at 0.3% and 0.4% shear strain for 30%, 50%, and 70% relative densities. From Fig. 7, it is observed that secant shear modulus increases up to 5000 cycles and remains almost constant thereafter. It is also observed that secant shear modulus due to an increase in relative density if the shear strain amplitude and confining pressure remains constant. If relative density increases, more soil particles are placed per unit volume of soil, thus increasing soil stiffness due to the strain cycle. The marginal reduction of damping ratio is observed at higher relative density (cf. Figure 8). For example, the shear modulus at the end of 10,000 cycle

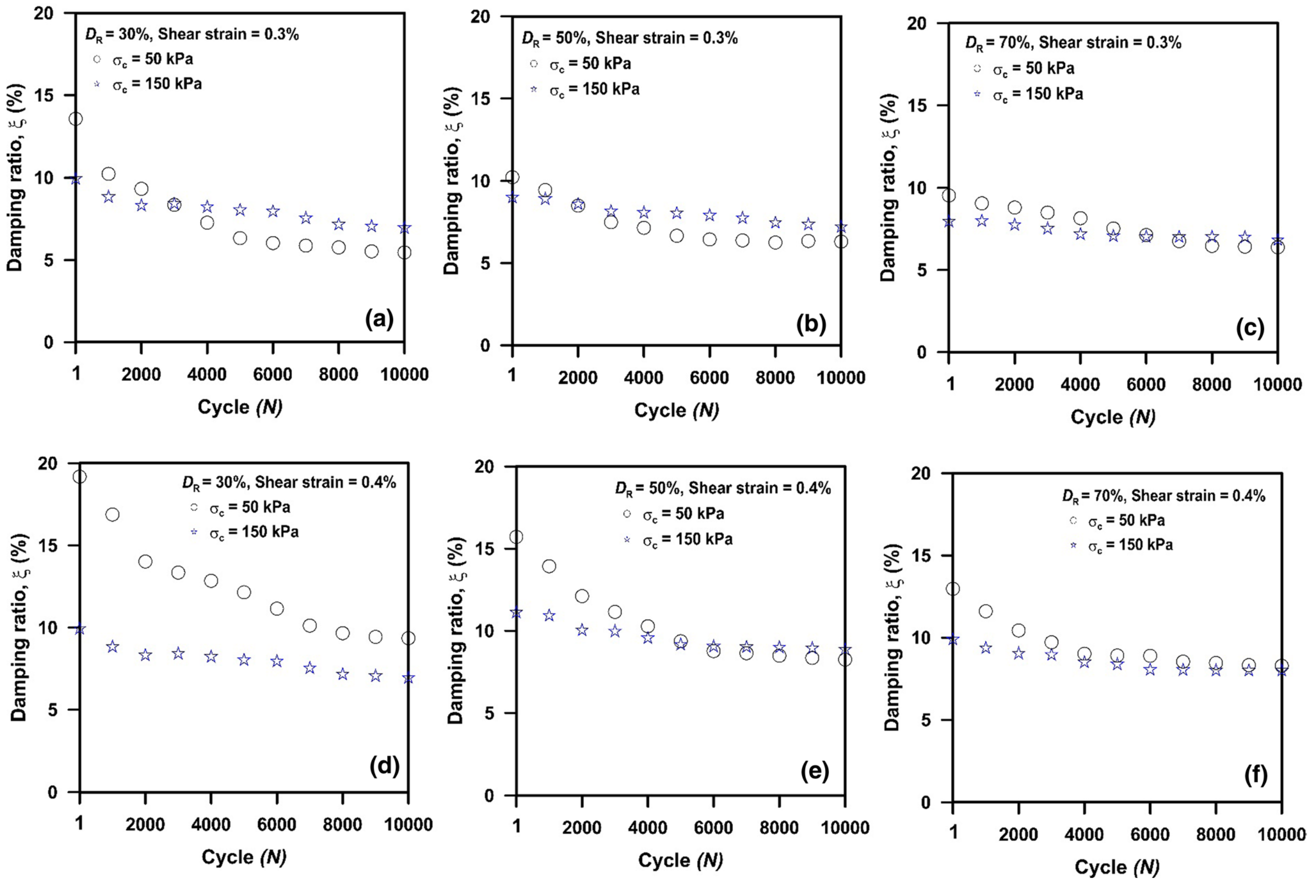

Fig. 6 Variation of damping ratio with cycle for **a** $D_R = 30\%$, **b** $D_R = 50\%$, and **c** $D_R = 70\%$ for shear strain $= 0.3\%$ and for **d** $D_R = 30\%$, **e** $D_R = 50\%$, and **f** $D_R = 70\%$ for shear strain $= 0.4\%$ at different confining pressures

are found to be 56,709 kPa, 64,942 kPa and 95,834 kPa for $D_R = 30\%$, 50% and 70%, respectively, at $\sigma_c = 50$ kPa and shear strain amplitude = 0.3% (Fig. 8a). The percentage increase of shear modulus at the end of 10,000 cycles is large at higher relative density (Fig. 7). For example, at $D_R = 70\%$, the percentage increase of secant shear modulus is found to be 56%, whereas the percentage increase of shear modulus is only 30% at $D_R = 50\%$ when the shear strain amplitude and effective confining pressure (σ_c) are 0.3% and 50 kPa, respectively (cf. Figure 7a). The reduction of damping ratio at the end of 10,000 cycles is observed to be 60% and 33% when the relative density (D_R) changes from 30 to 70% at $\sigma_c = 50$ kPa and shear strain amplitude = 0.3% (Fig. 8a).

3.1.3 Effect of Shear Strain Amplitude

Figure 9a–f summarizes the variation of secant shear modulus with the cycle at 50 kPa, 100 kPa, and 150 kPa effective confining pressures for 30%, and 70% relative densities at 0.3% and 0.4% of shear strain. Similarly, Fig. 10a–f summarizes the damping ratio variation with loading cycles at 50 kPa, 100 kPa, and 150 kPa effective confining pressures for 30%, and 70% relative densities at 0.3% and 0.4% of shear strain. From Fig. 9a–f, it is observed that if the effective confining pressure (σ_c) and relative density (D_R) remains constant, the shear modulus decreases if shear strain amplitude increases. For example, at $\sigma_c = 50$ kPa and $D_R = 30\%$, the secant shear modulus at the end of 5000 cycle is found to be 54,891 kPa and 44,282 kPa for shear strain rate 0.3% and 0.4%, respectively (cf. Figure 9a) and the damping ratio at the end of 5000 cycle at $\sigma_c = 50$ kPa and $D_R = 30\%$ is found to be 6.23% and 12.15% for shear strain rate 0.3% and 0.4%, respectively (cf. Figure 10a). When the shear strain rate increases, the movement of soil particles from its initial position increases, which results in a loose state of packing and an increase in the nonlinearity of the soil structure.

3.2 Post-Liquefaction Drained Behaviour of Silty Sand

The stress-controlled cyclic triaxial test is carried out at CSR = 0.1 and 0.2 to simulate the soil sample's liquefaction and determine the number of loading cycles required to liquefy the soil sample. The CSR for laboratory test

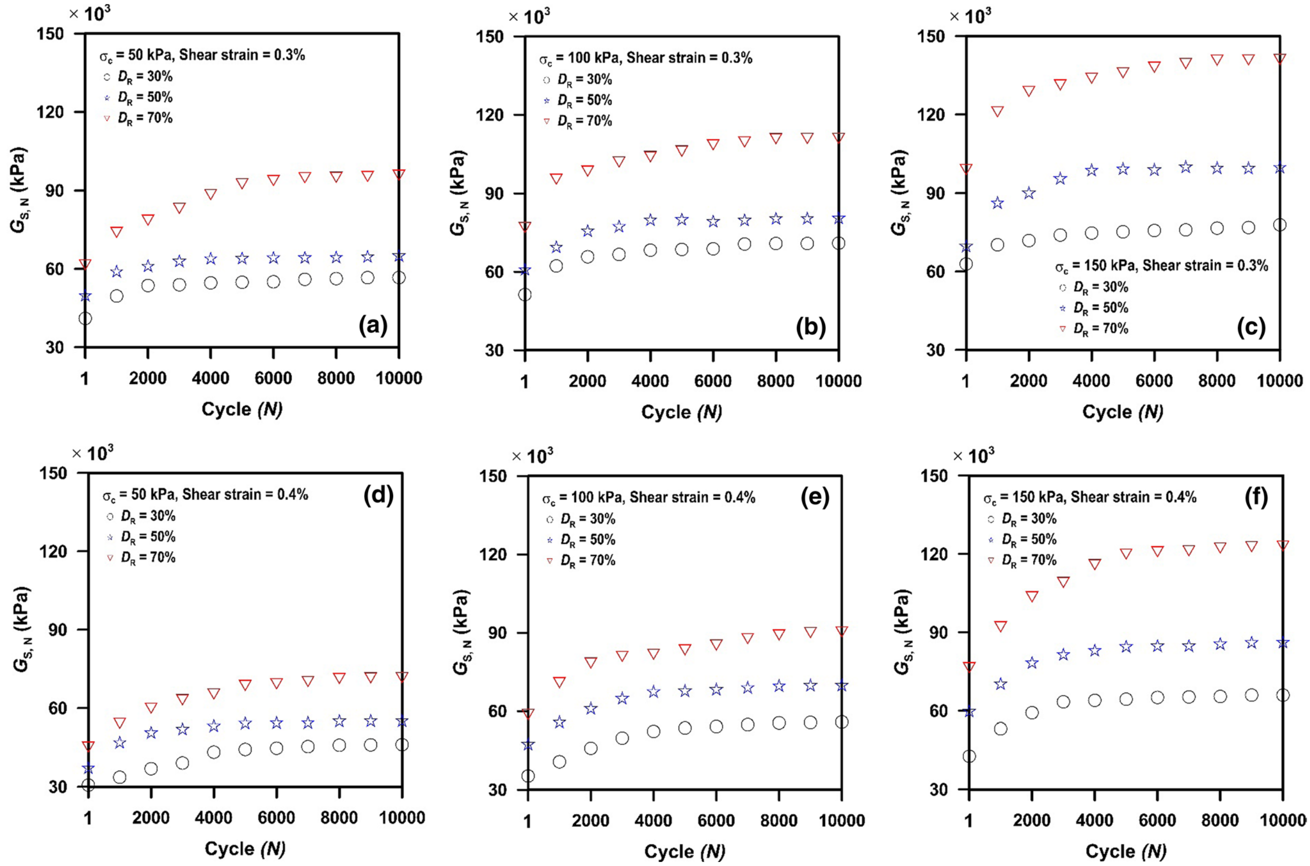

Fig. 7 Variation of shear modulus with cycle for **a** $\sigma_c = 50$ kPa, **b** $\sigma_c = 100$ kPa, and **c** $\sigma_c = 150$ kPa for shear strain = 0.3% and for **d** $\sigma_c = 50$ kPa, **e** $\sigma_c = 100$ kPa, and **f** $\sigma_c = 150$ kPa, for shear strain = 0.4% at different relative densities

condition (CSR_{tx}) is obtained from the field data, according to Kramer [39] as follows:

$$CSR_{\text{field}} = \frac{\tau_{cyc}}{\sigma'_v} = 0.9\, C_r CSR_{tx} \tag{4}$$

where CSR_{field} is the critical stress ratio in the field condition due to induced cyclic shear stress (τ_{cyc}) from a particular strong seismic ground motion. σ'_v is the effective vertical overburden pressure at a particular depth below the mudline level. C_r is a correction factor defined as follows (Finn et al. [45]):

$$C_r = (1 + K_0)/2 \tag{5}$$

K_0 is the coefficient of lateral earth pressure at rest, which equals to $1 - sin(\phi)$, where ϕ is the friction angle of soil. The silty sand's friction angle is estimated as 31° by performing the consolidated undrained (CU) triaxial test on silty sand at relative density equals to 30%. τ_{cyc} is estimated as follows (Seed and Idriss [46]:

$$\tau_{cyc} = 0.65\, \frac{a_{\max}}{g}\, \sigma_v\, r_d \tag{6}$$

where $a_{\max}$ is the peak ground acceleration (PGA) of the seismic strong ground motion record, σ_v is the total vertical stress at a particular depth below the mudline level, and r_d is the stress reduction factor according to Seed and Idriss [46]. Considering $a_{\max} = 0.1$ g, the CSR_{tx} varies from 0.15 to 0.2 up to a 10 m depth of soil below the mudline level having D_R varies in from 30 to 50%. Therefore, the tests are carried out at $CSR_{tx} = 0.1$ and 0.2 for an undrained test. As the objective of this test is to examine the post-liquefaction long-term drained behaviour, the stress-controlled cyclic triaxial tests at higher CSR values (i.e. $CSR_{tx} > 0.2$) were discarded as the liquefaction of the sample takes place within a few numbers of cycles.

Figure 11a, b, and c shows the variation of cyclic deviatoric stress, axial strain, and excess pore water pressure ratio with time, and Fig. 11d and e shows the variation of deviatoric stress versus shear strain for $CSR_{tx} = 0.2$, at σ_c =

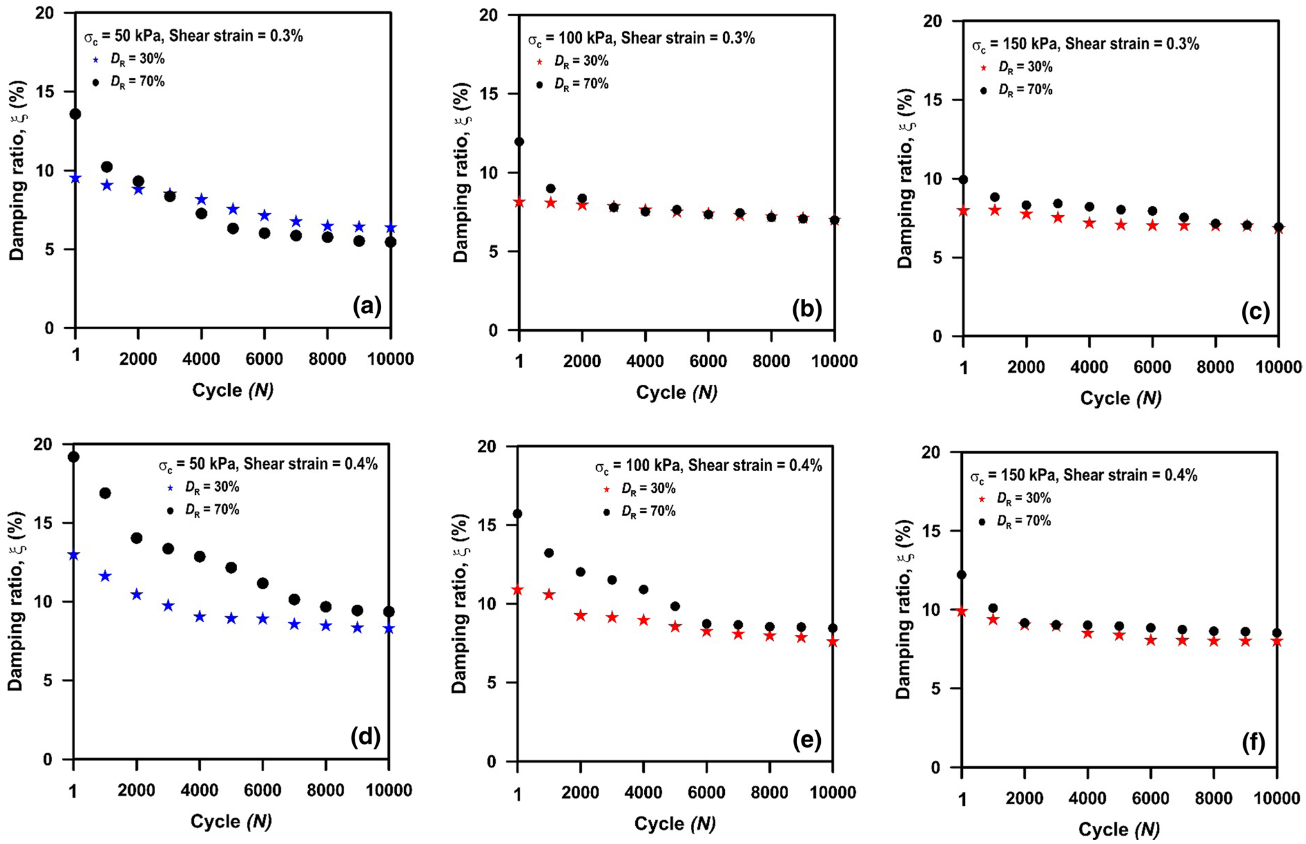

Fig. 8 Variation of damping ratio with cycle for **a** $\sigma_c = 50$ kPa, **b** $\sigma_c = 100$ kPa, and **c** $\sigma_c = 150$ kPa for shear strain = 0.3% and for **d** $\sigma_c = 50$ kPa, **e** $\sigma_c = 100$ kPa, and **f** $\sigma_c = 150$ kPa, for shear strain = 0.4% at different relative densities

50 kPa and $D_R = 30\%$. The results show that the excess pore water pressure ratio reaches 1.0 after 12 cycles of cyclic stress. The application of cyclic stress is stopped, and the drainage valve is opened soon after the excess pore pressure is reached 1.0, and the excess pore water pressure is allowed to release completely. The soil sample is kept undisturbed for 24 h after the complete release of excess pore water pressure. Thereafter, the strain-controlled cyclic triaxial test at a shear strain amplitude of 0.3% is carried out at drained condition to assess the post-liquefaction long-term behaviour. Figure 11f and g shows the hysteresis loop during the post-liquefaction state.

Figures 12a and b shows the variation of shear modulus with loading cycle for $D_R = 30\%$ and 50% for shear strain rate = 0.3% at effective confining pressure (σ_c) = 50 kPa for dry soil condition and during post-liquefaction stage. Similarly, Fig. 13a and b shows the variation of damping ratio with loading cycle for D_R = 30% and 50% for shear strain = 0.3% at effective confining pressure (σ_c) = 50 kPa for dry soil condition and during post-liquefaction stage. A marginal change of shear modulus and damping ratio with the loading cycle is observed during the post-liquefaction stage even if the soil samples are liquefied at different cyclic stress ratios (cf. Figs. 12 and 13). It means the cyclic stress ratio has a marginal effect on the post-liquefaction drained cyclic behaviour of silty sand. The shear modulus during post-liquefaction stage increases up to 2000 cycles and remains almost constant afterwards for $D_R = 30\%$, $\sigma_c = 50$ kPa and shear strain rate = 0.3% (cf. Fig. 12a). However, the shear modulus at any loading cycle during the post-liquefaction stage is found to be almost 33% lesser than the shear modulus during the dry state for the same test condition. When the soil liquefies, the disorientation of the soil particle (i.e. the soil particles move away from each other) occurs due to the rise of excess pore water pressure. The water present in the voids of soil solid pushes the soil solids away from each other, leading it to a less compact soil structure. Therefore, the shear modulus, i.e. shear strength of the soil after the first loading cycle, is less than the shear strength in the dry state. As soil particles move away from each other, resulting in a more nonlinear orientation of soil particles, the damping ratio increases during the post-liquefaction stage and can be observed from Fig. 13. However, the damping ratio at 50% relative density is found to be less than the damping ratio at 30% relative density of soil sample during the

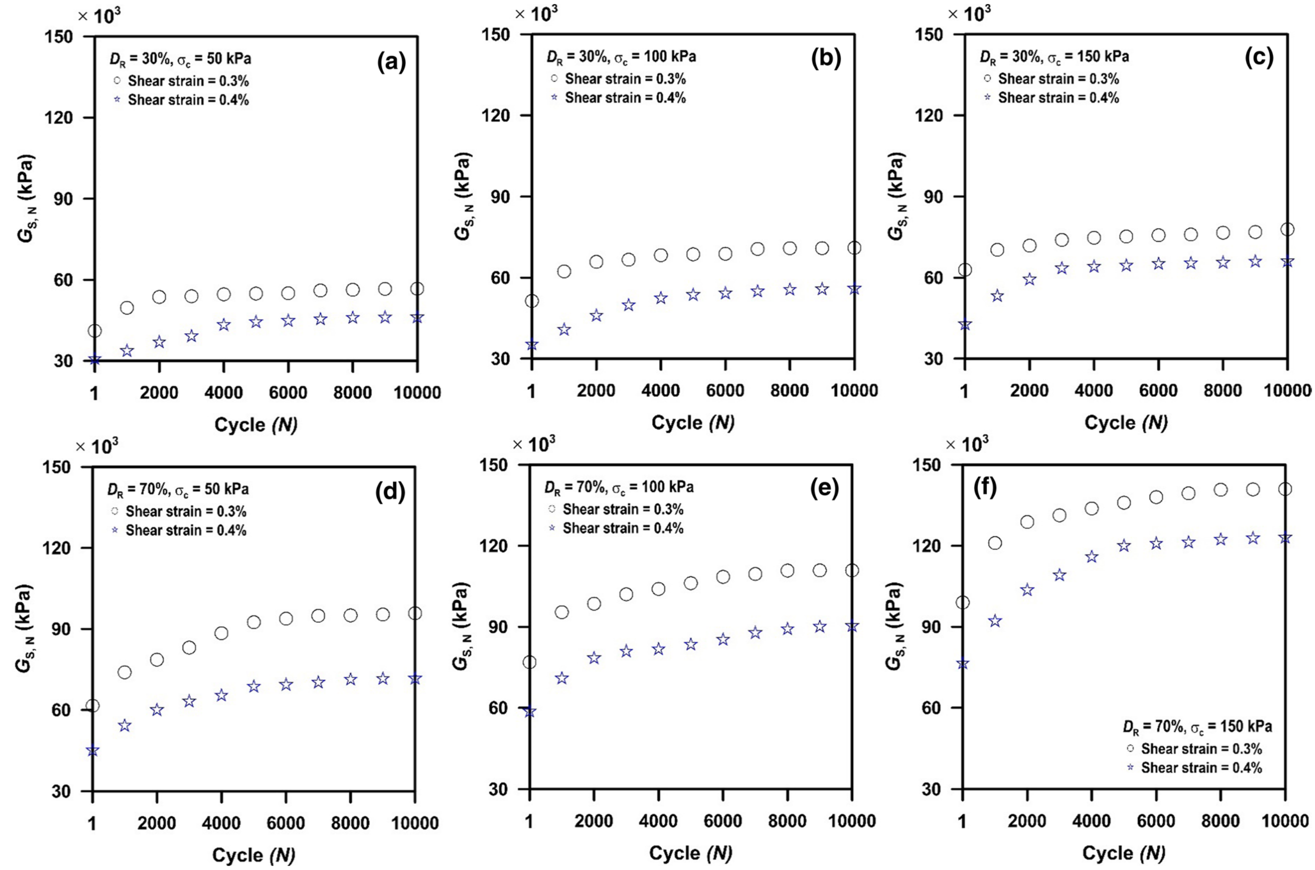

Fig. 9 Variation of shear modulus with cycle for **a** $\sigma_c = 50$ kPa, **b** $\sigma_c = 100$ kPa, and **c** $\sigma_c = 150$ kPa for $D_R = 30\%$ and for **d** $\sigma_c = 50$ kPa, **e** $\sigma_c = 100$ kPa, and **f** $\sigma_c = 150$ kPa, for $D_R = 70\%$ for shear strain rate equals to 0.3% and 0.4%

post-liquefaction stage due to more linear orientation of soil particle at higher relative density.

The shear modulus increases continuously up to 2000 cycles and remains constant afterwards during the post-liquefaction stage for $D_R = 30\%$, $\sigma_c = 50$ kPa, and shear strain rate = 0.3%. As the test is carried out under drained conditions during the post-liquefaction stage, there is no chance to increase pore water pressure. Due to cyclic shear strain's continuous application during the post-liquefaction stage, the soil particles again come closer to each other and finally arranged in a more stable oriented state. Therefore, after 2000 loading cycle the shear modulus and damping ratio remains almost constant for $D_R = 30\%$, $\sigma_c = 50$ kPa and shear strain rate = 0.3% (cf. Figs. 12 and 13a). It is interesting to observe from Fig. 12b that the shear modulus is found to be less than the shear modulus at dry state up to 4000 load cycles, and increases up to 8000 cycles and remains constant afterwards for $D_R = 50\%$, $\sigma_c = 50$ kPa and shear strain rate = 0.3%. After 4000 load cycles, the shear modulus remains higher than the shear modulus at a dry state for the same testing condition. It may be due to the soil sample's reconsolidation and densification effect at medium relative density [47].

3.3 Development of Numerical Model and Implication in OWT Design

The OWT system's natural frequency is a part of design calculation to avoid accidental resonance and associated effects, such as early fatigue damage. Offshore wind turbine structures are usually subjected to a wide frequency range due to wind turbulence, wave, mass imbalance (1P), and tower shadowing load (3P). Hence, the prediction of temporal variation of the natural frequency is essential to ensure that the forcing frequencies high energy level do not coincide with OWT's natural frequency (IPWIND 2011). The overall frequency of OWT is derived based on the proposed numerical model as follows:

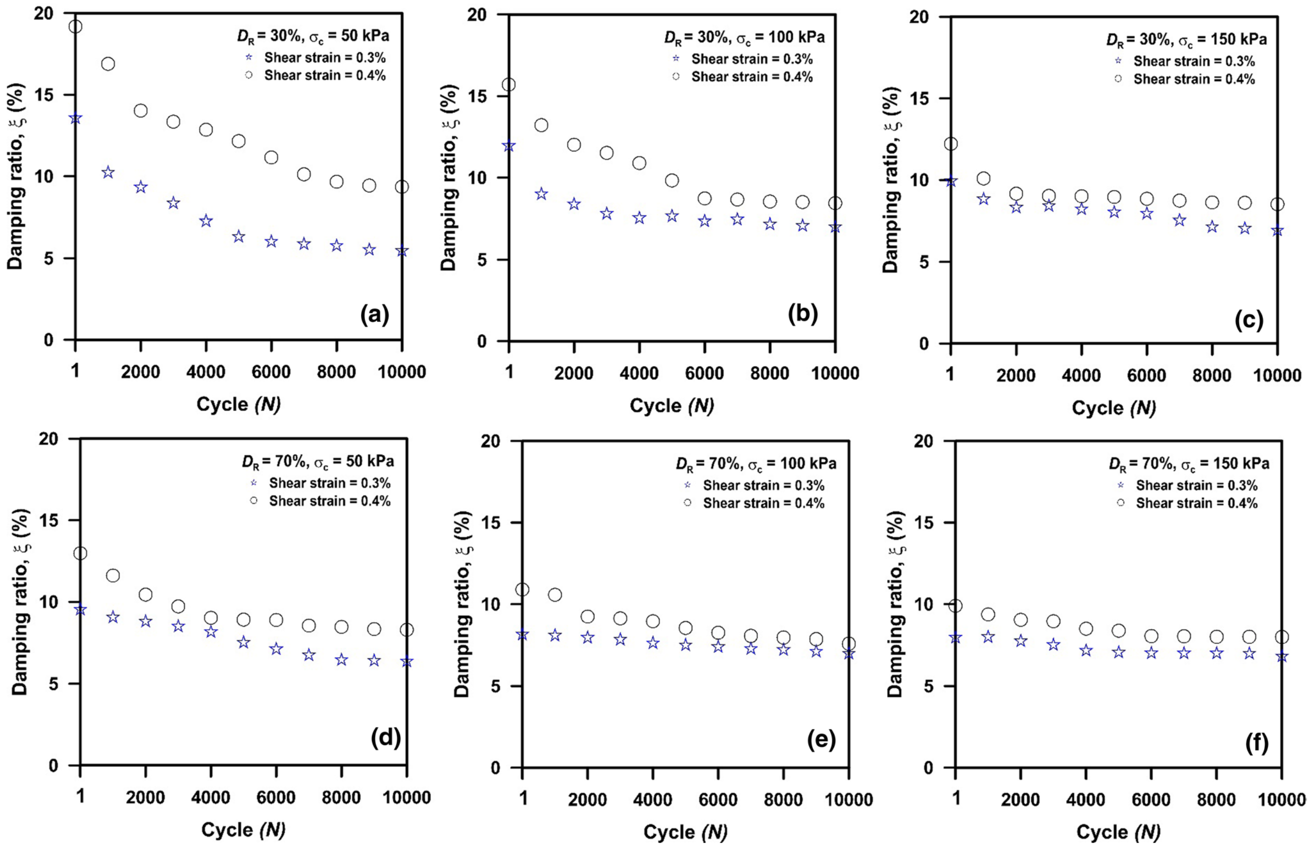

Fig. 10 Variation of damping ratio with cycle for **a** $\sigma_c = 50$ kPa, **b** $\sigma_c = 100$ kPa, and **c** $\sigma_c = 150$ kPa for $D_R = 30\%$ and for **d**$\sigma_c = 50$ kPa, **e** $\sigma_c = 100$ kPa, and **f** $\sigma_c = 150$ kPa, for $D_R = 70\%$ for shear strain rate equals to 0.3% and 0.4%

3.3.1 Description of Numerical Model

A two-dimensional (2D) beam on a nonlinear Winkler foundation (BNWF) model as shown in Fig. 14 is formulated using *OpenSees* [48, 49] to predict the variation of the natural frequency of Vestas V90-3.0 MW [4] OWT during operational, liquefaction and post-liquefaction phase based on the cyclic triaxial test results. The monopile is assumed to be embedded in three layered silty sand deposit where the top layer consists of loose silty sand having relative density (D_R), and thickness (h_1) equals to 30% and 5 m overlain by a layer of medium dense silty sand having $D_R = 50\%$ and $h_2 = 10$ m at the middle, and the bottom layer consists of dense silty sand having $D_R = 70\%$ and $h_2 = 13$ m. Mean sea level (MSL) height is assumed to be 5 m above the mud line level.

The monopile, transition piece, and tower are modelled using a linear beam-column element with structural properties similar to Vestas V90-3.0 MW OWT. The properties of Vestas V90-3.0 MW OWT is listed in Table 4. The cross-section for the monopile (i.e. from pile tip to mean sea level) is assumed to be uniform and is modelled as a series of interconnecting displacement-based beam-column elements. The tapered tower is modelled as several segments connected according to continuity condition, and each segment follows characteristics of uniform cross-section [50, 51]. Each monopile and tower node is defined with a single lumped mass and rotary inertia. Each tower and pile node has two translational and one rotational degree of freedom. The Rotor Nacelle Assembly (RNA) is modelled as a lumped mass (M_{RNA}) at the tower top with rotary inertia (J_{RNA}). Vertical movement of all pile and tower nodes are restricted in this study. Based on the convergence study, a segmental length of both tower and monopile is fixed to be 0.5 m.

Spring elements are used to characterize the lateral resistance between soil and pile. *The elastic uniaxial* material object in *OpenSees* is used to represent the constitutive behaviour of spring. Parameter, such as an elastic modulus, is required to define the constitutive behaviour of *Elastic uniaxial* material. The elastic modulus is computed from the cyclic triaxial test and is applied as input (i.e. elastic modulus) to the FE model to predict the OWT system's natural frequency. The springs are generated using *Zero-length* elements, which are characterized by *Elastic uniaxial* material to represent stress–strain behaviour in the horizontal direction. These spring nodes are created with two

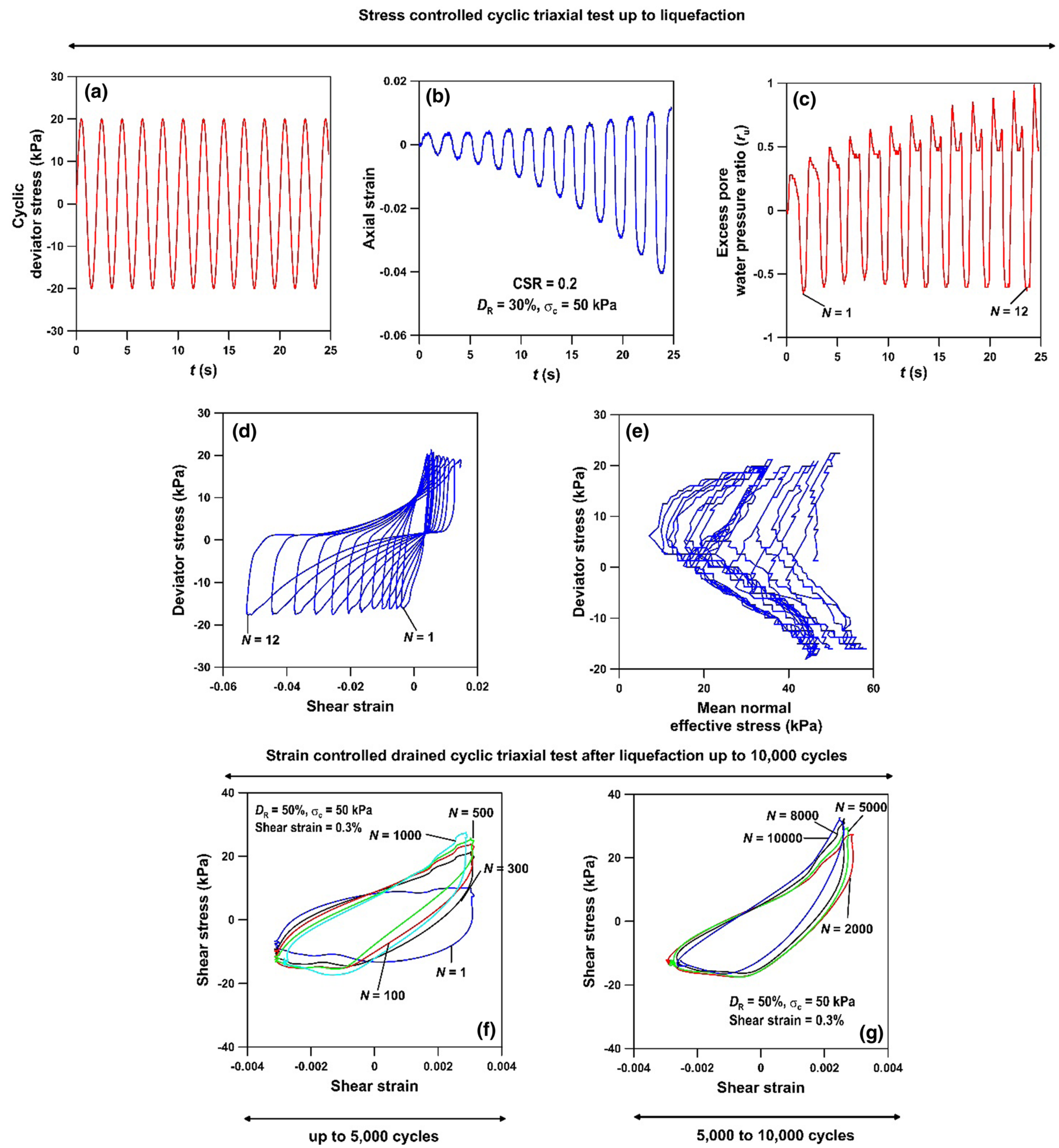

Fig. 11 Variation of **a** cyclic deviatroic stress **b** axial strain **c** excess pore water pressure ratio **d** variation of deviatroic stress verses shear strain up to liquefaction) stress path at CSR = 0.2, and variation of shear stress versus shear strain up to **f** 5000 cycles and **g** 5000 to 10,000 cycles during post-liquefaction stage at shear strain rate 0.3% for $\sigma_c = 50$ kPa and $D_R = 30\%$

dimensions with three translational degrees-of-freedom over the pile's embedded depth. Two more nodes are defined at the location of each pile nodes to assign the zero-length elements. Since Zero-length elements are used for the springs, one of the spring nodes is fixed in all three translational degrees-of-freedom, and the other spring node, i.e. the slave node, is connected to the pile nodes. The numerical model is used to analyse the influence of the temporal variation of soil stiffness on the first and second natural frequencies of the OWT system at the operational phase, liquefaction

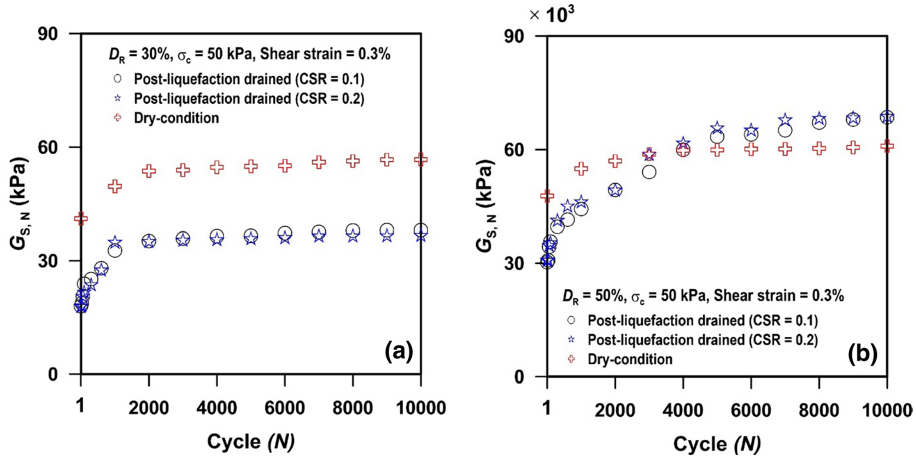

Fig. 12 Variation of shear modulus with cycle for **a** $D_R = 30\%$, **b** $D_R = 50\%$ for shear strain = 0.3%, effective confining pressure (σ_c) = 50 kPa during dry condition and post-liquefaction stage

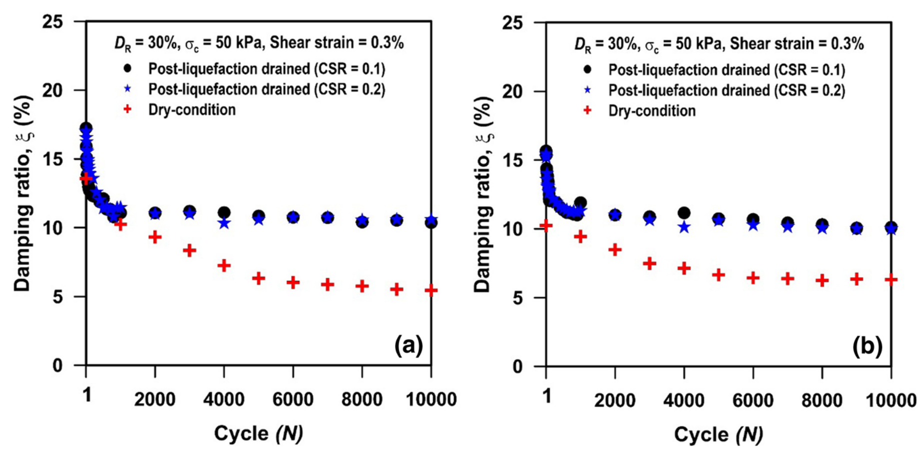

Fig. 13 Variation of damping ratio with cycle for **a** $D_R = 30\%$, **b** $D_R = 50\%$ for shear strain = 0.3%, effective confining pressure (σ_c) = 50 kPa during dry condition and post-liquefaction stage

phase, and post-liquefaction phase. The variation of soil spring stiffness (K) is assumed to vary with the number of load cycles according to the variation of shear modulus at different load cycles as observed in element tests. An Eigen analysis is carried during the operational, liquefaction, and post-liquefaction phase to investigate the impact of stiffness improvement and degradation on the fundamental frequency of the OWT structure.

3.3.2 Variation of Soil Stiffness During Operational and Post-Liquefaction Phase

The average effective confining pressure on the soil element surrounding the monopile at the topsoil layer is assumed to be 50 kPa, and the soil is particularly loose silty sand having a relative density (D_R) equals to 30%. The average effective confining pressure on the soil element surrounding the monopile in the middle and the bottom layer is assumed to be 100 kPa and 150 kPa, respectively, and the relative densities of these layers are assumed to be 50% and 70%, respectively. The variation of soil stiffness at the operational condition with load cycles at three different soil layers is considered the same as that of variation of shear modulus from the element test shown in Fig. 6. The variation of non-dimensional stiffness (i.e. the ratio of stiffness at the Nth cycle (K_N) to the initial stiffness (K_0)) for the soil element in all three layers for all relative densities and confining pressures are plotted in Fig. 15. It is observed from Fig. 15a that all the curves merged and the non-dimensional stiffness evolve approximately logarithmically with load cycle numbers as:

$$K_N/K_0 = 0.048\ln(N) + 1 \tag{7}$$

At the liquefaction phase, it is assumed that the top 10 m soil consisting of loose silty sand is liquefied during a seismic event. The stiffness of soil spring at a different stage of liquefaction is considered as a stiffness multiplier method. This means that the stiffness of soil spring is scaled by a factor and subjected to a minimum stiffness of $0.1K_0$ [52] as given below:

$$K_N/K_0 = \max\{(1 - r_u(N)), 0.1\} \tag{8}$$

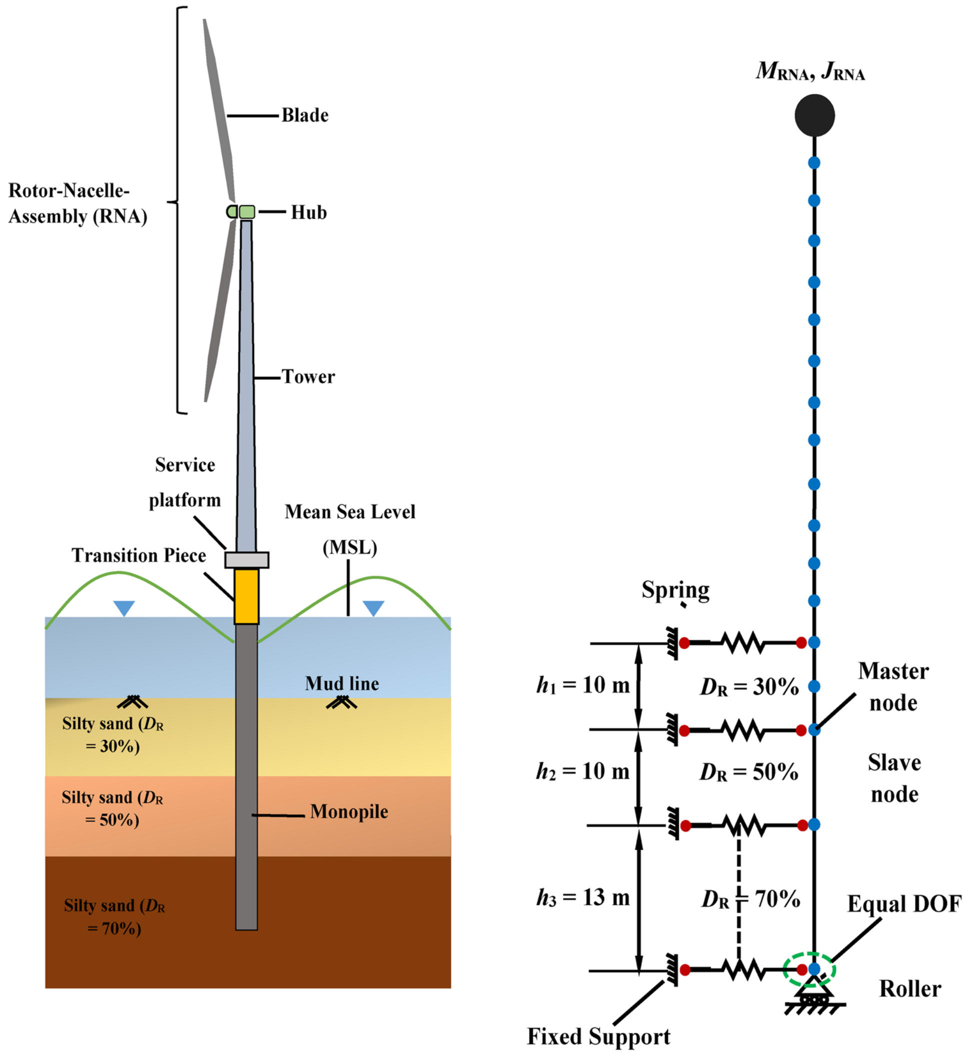

Fig. 14 Schematic diagram of the proposed two-dimensional finite element model

where $r_u(N)$ The excess pore water pressure ratio as a function of load cycles (N). The reduction of stiffness is estimated based on the excess pore water pressure developed at various load cycles, as illustrated in Fig. 11 a. The variation of K_N/K_0 during the post-liquefaction phase is shown in Fig. 15b. It is observed from Fig. 15b that K_N/K_0 varies logarithmically with the loading cycle, and the slope is independent of the cyclic stress ratio (CSR). The non-dimensional soil stiffness can be approximated as:

$$K_N/K_0 = 0.15\ln(N) + 1 \tag{9}$$

The variation of stiffness at the post-liquefied phase (i.e. Eq. (9)) is pertinent to the liquefied soil layer. The fitted equations are in line with the soil-stiffening model proposed by Leblanc et al. [8] for sand. Note that the initial soil stiffness (K_0) for three different soil layers is estimated from API [26] for the assumed relative densities of soil.

3.3.3 Long-Term Variation of the Natural Frequency of OWT

The fundamental frequency of the soil–monopile–tower system is generally kept sufficiently away from the operating frequencies (i.e. 1P frequency and 3P frequency) of the OWT system to avoid resonance [7]. It is also reported that dynamic amplification due to 1P and 3P is of the highest order than wind and wave loading [53]. Resonance is also reported due to operational wind farms in the German North Sea [54]. The operating frequency (f_r) of the Vestas V90-3.0 MW is 0.06–0.23 Hz [55]. The resonance condition can be avoided by keeping the fundamental frequency of the OWT system ± 10% away from the rotor frequency (1P) and blade passing frequency (3P) (DNV-GL-ST-0126, [12]. The natural frequency of the OWT structure strongly depends on the stiffness of the soil surrounding the monopile. Figure 16a and b shows the variation of the first (f_{n1}) and second

Table 4 Properties of Vestas V90 3 MW OWT [4]

Characteristic	Value
Rotor radius	45 m
Tower length	80 m
Tower mass	145 t
Tower base diameter	4.20 m
Tower top diameter	2.31 m
Tower second moment of area	0.5702 m^4
Tower Young's modulus	210 GPa
Tower flexural rigidity	1.20×10^{11} Nm^2
Monopile length	28 m
Monopile diameter	4.3 m
Monopile wall thickness	45 mm
Monopile mass	132 t
Monopile Young's modulus	210 GPa
Monopile second moment of area	1.3615 m^4
Monopile flexural rigidity	2.86×10^{11} Nm^2
Rotor-nacelle mass	111 t
Rotor operational Interval	8.6-18.4 rpm

natural (f_{n2}) frequency during the operational, liquefaction, and post-liquefaction phase. It is observed from Fig. 16 that both first and second natural frequencies increase up to 5000 cycles, and thereafter the rate of increase decreases during the operational phase. This is due to the densification effect of the soil surrounding the monopile. The initial first and second natural frequencies of Vestas V90-3.0 MW are found to be 0.353 Hz and 2.293 Hz, respectively. At the end of the 10,000 loading cycle, an increase of 1.6% and 2.3% is observed in first and second natural frequencies, respectively. When a certain depth of soil surrounding the monopile liquefies during any seismic event, the stiffness of that liquefied layer decreases drastically. It causes a decrease in the overall stiffness of the OWT system and hence causes a decrease in the fundamental frequency of the OWT system. Both first and second natural frequencies decreased from 0.357 to 0.32 Hz and 2.334 to 2.0 Hz, respectively, during the liquefaction phase. Post-liquefaction excess pore water pressure dissipation causes the densification of the soil surrounding the monopile. Hence, the soil deposit in the liquefied layer starts gaining strength and stiffness. Therefore, both first and second natural frequencies again start

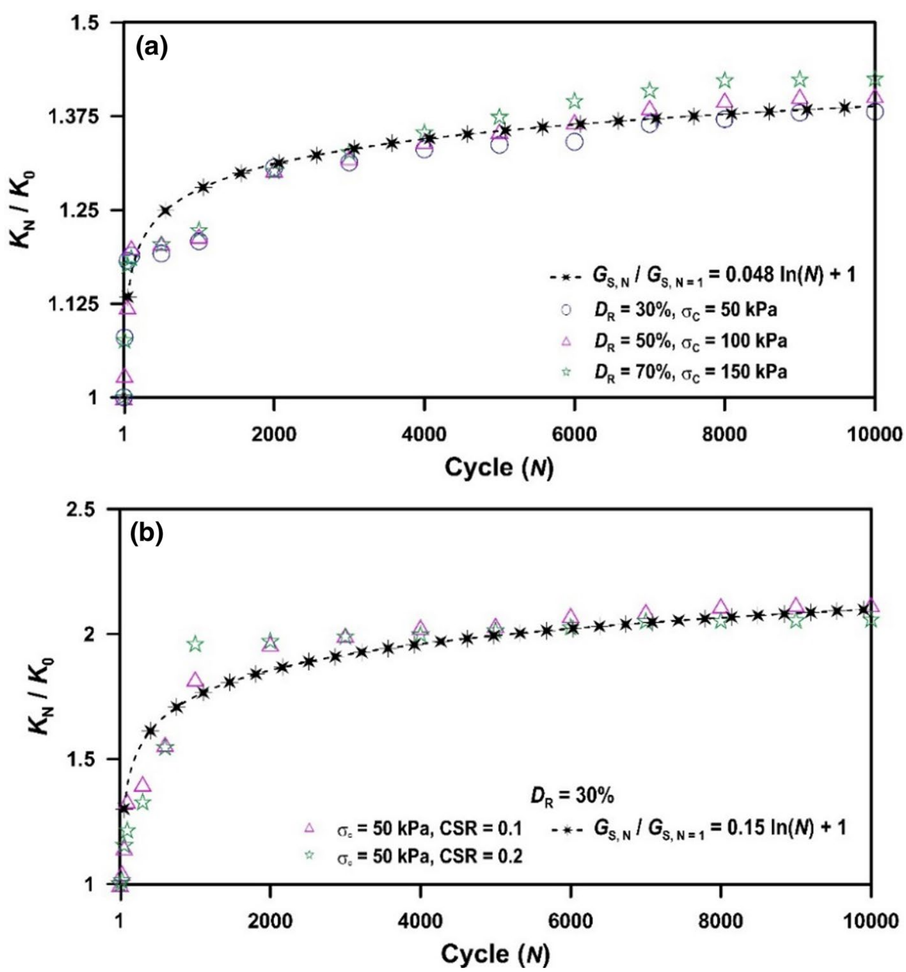

Fig. 15 Variation of non-dimensional stiffness with load cycle during **a** operational phase and **b** during post-liquefaction phase

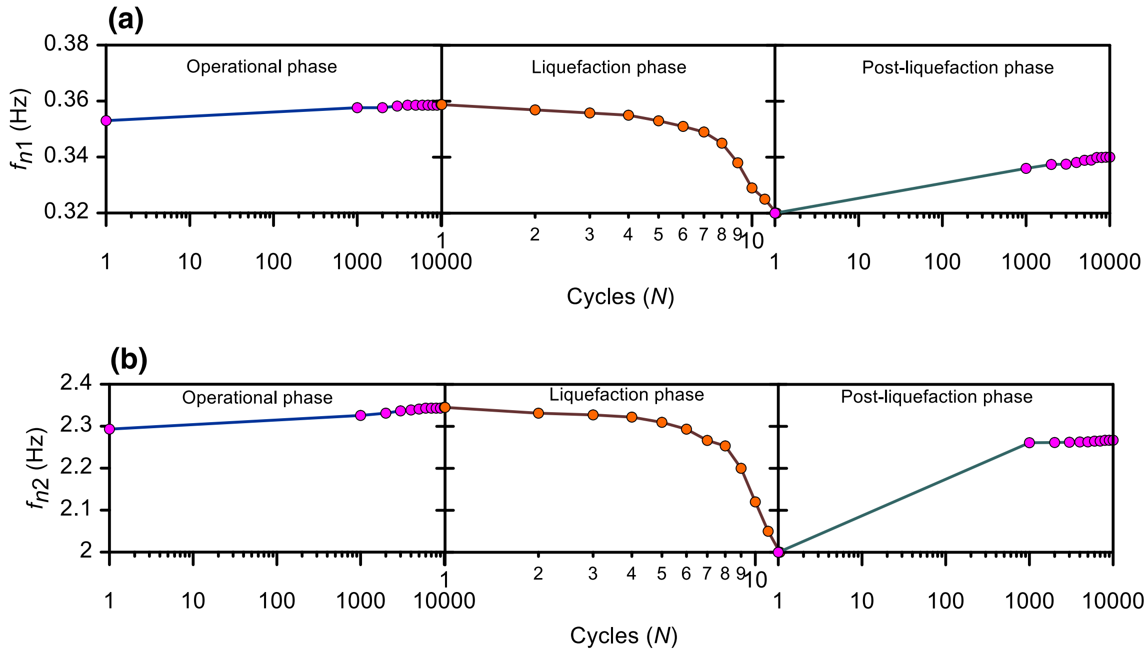

Fig. 16 Variation of **a** first natural frequency and **b** second natural frequency during operational, liquefaction, and post-liquefaction phase

increasing, and the rate of increase decreases after specific cycles. However, the total gain of strength is not achieved after liquefaction; hence, the fundamental frequency lies below the operational phase's fundamental frequency. The first natural frequency increases from 0.32 to 0.34 at the end of the 10,000-loading cycle during the post-liquefaction phase (cf. Fig. 16a). A similar trend is also observed in the second natural frequency of OWT, as shown in Fig. 16b. Therefore, the stiffening of OWT's natural frequency is observed over time and shifts towards 3P frequency at the operational condition. Stiffening of second natural frequency is more than that of first natural frequency. A drastic reduction in natural frequency happens due to soil liquefaction; however, it gradually stiffens at the post-liquefaction phase. Typical first and second mode shapes of the OWT structure are shown in Fig. 17 during the operational, liquefaction, and post-liquefaction phases.

A typical estimate suggests that OWT foundations are subjected to at least 100 million load cycles over 25 years design period [9]. Hence, considering 4 million load cycles per year, the first natural frequency of Vestas V90-3.0 MW is forecasted for four years period and presented in Fig. 18. About a 3% increase in first natural frequency is observed over 4 years. The monitoring data of a 3 MW OWT of Belwind Offshore Wind Farm in the Flemish Banks area of the southern North Sea off the Belgian coast installed in sandy soil also show an increase of first-order resonance frequency is about 4.6% (cf. Fig. 16) during its four-year operational period [56]. It corroborates the densification of sand during its operational period.

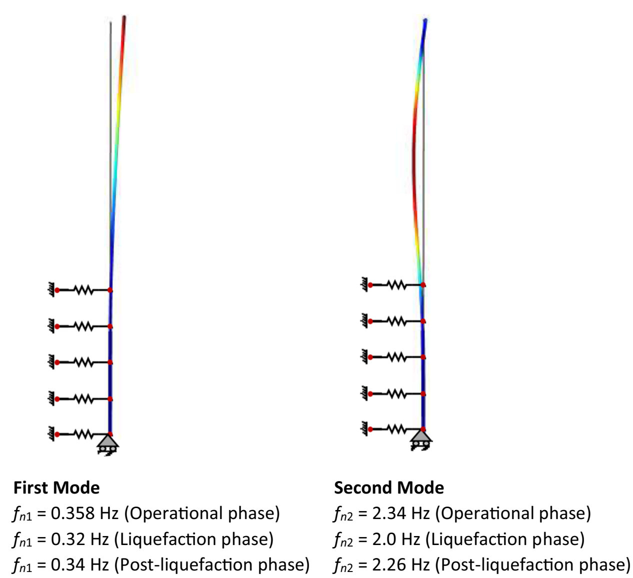

Fig. 17 Mode shapes of OWT structure during operational, liquefaction, and post-liquefaction phase

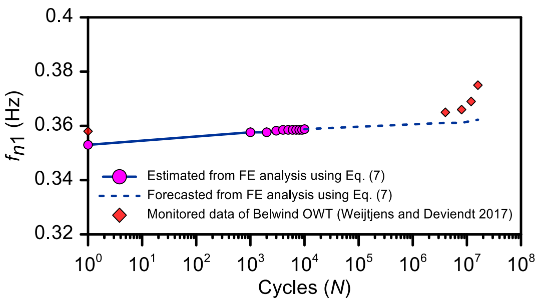

Fig. 18 Predicted and forecasted first natural frequency of Vestas V90-3.0 MW OWT using FE analysis and measured first natural frequency from 2012–2016 of Belwind OWT at the operational condition

4 Conclusion

The long-term cyclic behaviour of silty sand is studied during the operational, liquefaction, and post-liquefaction stage by performing a series of strain/stress-controlled cyclic triaxial tests under the drained/undrained condition up to 10,000 cycles. The effect of relative density, effective confining pressure, and shear strain rate on the dynamic soil properties such as secant shear modulus and damping ratio is also studied, and a comparison of shear modulus and damping ratio during pre-liquefaction and post-liquefaction stage is made. Based upon the experimental observation, a numerical model showing the variation of shear modulus is developed and is used as an input to the 2D-BNWF model formulated in *OpenSees* to predict the long-term variation of the fundamental frequency of the OWT structure in various phases. Following conclusions are drawn based on experimental and numerical observations:

1. The shear modulus increases, and the damping ratio decreases up to 5000 load cycles and remains almost constant thereafter during dry test conditions. It is due to the densification effect of silty sand due to the application of the cyclic load.
2. Shear modulus increases if relative density increases at a constant effective confining pressure and shear strain rate in both pre-liquefaction and post-liquefaction stage, and less change in damping ratio is observed at higher relative density due to dense and compacted soil structure.
3. Shear modulus increases and change in damping ratio is less at higher effective confining pressure if relative density and shear strain rate remain constant.
4. Shear modulus decreases, and the damping ratio increases if the shear strain rate increases while relative density and effective confining pressure remain constant. It is due to an increase in looseness and nonlinearity of the soil structure at a higher strain rate.
5. The critical stress ratio (CSR) has a marginal effect on the silty sand's post-liquefaction dynamic behaviour. The shear modulus at any load cycle is found to be less than the shear modulus during a dry state when the soil samples are loose, i.e. $D_R = 30\%$. However, during the post-liquefaction stage, the shear modulus is higher than the shear modulus during dry state after 4000 load cycles when $D_R = 50\%$ due to the reconsolidation effect.
6. Numerical study indicates the soil stiffness varies logarithmically with the loading cycle in both liquefaction and post-liquefaction phase, and the slope of the stiffness curve is independent of relative density, confining pressure, and cyclic stress ratio.
7. The fundamental frequency (i.e. both first order and second order) increases during the operational and post-liquefaction phase for a particular cycle, and the rate of increase decreases thereafter. It is due to the densification effect of the soil surrounding the monopile. This aspect is vital for the design of OWT to avoid resonance due to 1P and 3P loading.

Acknowledgements The authors are thankful to the anonymous reviewers for their critical comments, which have helped improve the work.

References

1. Cui, L.; Bhattacharya, S.: Soil–monopile interactions for offshore wind turbines. Proc. Instit. Civil Eng. Eng. Comput. Mech. **169**(4), 171–182 (2016)
2. Westgate Z.J.; DeJong J.T.: Geotechnical considerations for offshore wind turbines. Report for MTC OTC Project 2005
3. Kuo, Y.S.; Achmus, M.; Abdel-Rahman, K.: Minimum embedded length of cyclic horizontally loaded monopiles. J. Geotech. Geoenviron. Eng. **138**(3), 357–363 (2012)
4. Lombardi, D.: Dynamics of offshore wind turbines. Ph.D. thesis. U. K.: University of Bristol; 2010.
5. Schaumann, P.; Lochte-Holtgreven, S.; Steppeler, S.: Special fatigue aspects in support structures of offshore wind turbines. Mater. Sci. Technol. **42**(12), 1075–1081 (2011)
6. Lombardi, D.; Bhattacharya, S.; Wood, D.M.: Dynamic soil–structure interaction of monopile supported wind turbines in cohesive soil. Soil Dyn. Earthq. Eng. **49**, 165–180 (2013)
7. Bisoi, S.; Haldar, S.: Dynamic analysis of offshore wind turbine in clay considering soil–monopile–tower interaction. Soil Dyn. Earthq. Eng. **63**, 19–35 (2014)
8. LeBlanc, C.: Design of offshore wind turbine support structures. Ph.D. thesis. Denmark: Aalborg University; (2009)
9. Nikitas, G.; Arany, L.; Aingaran, S.; Vimalan, J.; Bhattacharya, S.: Predicting long term performance of offshore wind turbines using cyclic simple shear apparatus. Soil Dyn. Earthq. Eng. **92**, 678–683 (2017)

10. Zaaijer, M.B.: Foundation modelling to assess dynamic behaviour of offshore wind turbines. Appl. Ocean Res. **28**(1), 45–57 (2006)
11. Bhattacharya, S.; Nikitas, N.; Garnsey, J.; Alexander, N.A.; Cox, J.; Lombardi, D.; Wood, D.M.; Nash, D.F.: Observed dynamic soil–structure interaction in scale testing of offshore wind turbine foundations. Soil Dyn.Earthq. Eng. **54**, 47–60 (2013)
12. DNVGL-ST-0126. Design of offshore wind turbine structures. DET NORSKE VERITAS; (2016)
13. Risi, D.R.; Bhattacharya, S.; Goda, K.: Seismic performance assessment of monopile-supported offshore wind turbines using unscaled natural earthquake records. Soil Dyn. Earthq. Eng. **109**, 154–172 (2018)
14. Ghosh B.; Peiris N.; Lubkowski Z.: Assessment of seismic risk for the design of offshore structures in liquefiable soil. In: proceeding of 4th International Conference on Earthquake Geotechnical Engineering (2007)
15. Wang, P.; Li, Q.; Li, C.F.: Sedimentology. In: Wang, P.; Li, Q.; Li, C.F. (eds.) Developments in Marine Geology, vol. 6, pp. 183–340, Elsevier (2014)
16. Gulhati, S. K.: Geotechnical Aspects of the Indian offshore environment. In: 31st Annual General Session, Indian Geotechnical Conference, Visakhapatnam, India
17. Son, S.W.; Ko, M.J.; Kim, J.M.: Cyclic shear behavior characteristics of marine silty sand. J. Mar. Sci. Technol. **25**(6), 784–790 (2017)
18. Bhattacharya, S.; Lombardi, D.; Wood, D.M.: Similitude relationships for physical modelling of monopile-supported offshore wind turbines. Int. J. Phys. Modell. Geotech. **11**(2), 58–68 (2011)
19. Cox, J.; Jones, C.: Long term performance of suction caisson supported offshore wind turbines. Struct. Eng. **89**(19), 12–13 (2011)
20. Ma, H.; Yang, J.; Chen, L.: Numerical analysis of the long-term performance of offshore wind turbines supported by monopiles. Ocean Eng. **136**, 94–105 (2017)
21. Abhinav, K.A.; Saha, N.: Dynamic analysis of monopile supported offshore wind turbines. Proc. Instit. Civil Eng. Geotech. Eng. **170**(5), 428–444 (2017)
22. Wang, X.; Yang, X.; Zeng, X.: Lateral response of improved suction bucket foundation for offshore wind turbine in centrifuge modelling. Ocean Eng. **141**, 295–307 (2017)
23. Duan, N.; Cheng, Y.P.; Xu, X.: Distinct-element analysis of an offshore wind turbine monopile under cyclic lateral load. Proc. Instit. Civil Eng.-Geotech. Eng. **170**(6), 517–533 (2017)
24. Bhattacharya, S.; Adhikari, S.: Experimental validation of soil–structure interaction of offshore wind turbines. Soil Dyn. Earthq. Eng. **31**(5–6), 805–816 (2011)
25. Cuéllar, P.; Georgi, S.; Baeßler, M.; Rücker, W.: On the quasi-static granular convective flow and sand densification around pile foundations under cyclic lateral loading. Granul. Matter **14**(1), 11–25 (2012)
26. API-RP-2GEO: Geotechnical and Foundation Design Considerations. American Petroleum Institute, Washington (2011)
27. Weijtjens W, Verbelen T, Devriendt C. Temporal evolution of stiffness for offshore monopile foundations. In: Proceedings of Offshore Wind Energy Conference 2017; London.
28. Arany, L.; Bhattacharya, S.; Macdonald, J.; Hogan, S.J.: Design of monopiles for offshore wind turbines in 10 steps. Soil Dyn. Earthq. Eng. **92**, 126–152 (2017)
29. Lombardi, D.; Dash, S.R.; Bhattacharya, S.; Ibraim, E.; Muir Wood, D.; Taylor, C.A.: Construction of simplified design p–y curves for liquefied soils. Géotechnique **67**(3), 216–227 (2017)
30. Nozu, A.; Ichii, K.; Sugano, T.: Seismic design of port structures. J. Jpn Assoc. Earthq. Eng. **4**(3), 195–208 (2004)
31. Standard-IS, Indian. IS 2720 (Part 3) 1980. Methods of test for soils, determination of specific gravity, fine, medium and coarse grained soils, New Delhi.
32. Standard-IS, Indian. IS 2720 (Part 14) 2006. Methods of Test for Soils–Determination of Density Index for Cohesionless Soils.
33. Iwasaki, T.; Tatsuoka, F.; Takagi, Y.: Shear moduli of sands under cyclic torsional shear loading. Soils Found. **18**(1), 39–56 (1978)
34. Hardin, B.O.: The nature of damping in sands. J. Soil Mech. Found. Div. **92**(5), 490 (1965)
35. Kokusho, T.: Cyclic triaxial test of dynamic soil properties for wide strain range. Soils Found. **20**(2), 45–60 (1980)
36. Lin, M.L.; Huang, T.H.; You, J.C.: The effects of frequency on damping properties of sand. Soil Dyn. Earthq. Eng. **15**(4), 269–278 (1996)
37. Orfanidis, S.J.: Introduction to signal processing. Prentice-Hall, Englewood Cliffs, NJ (1996)
38. Schafer, R.W.: What is a Savitzky-Golay filter? (lecture notes). IEEE Signal Process. Mag. **28**(4), 111–117 (2011)
39. Kramer, S.L.: Geotechnical Earthquake Engineering. Prentice Hall, New Jersey (1996)
40. Ravishankar B.V.; Sitharam T.G.; Govindaraju L.: Dynamic properties of Ahmedabad sands at large strains. In: Proceedings of Indian Geotechnical Conference 2005; pp. 17–19
41. Rollins, K.M.; Evans, M.D.; Diehl, N.B.: Shear modulus and damping relationships for gravels. J. Geotech. Geoenviron. Eng. **124**(5), 396–405 (1998)
42. Chung, R.M.; Yokel, F.Y.; Drnevich, V.P.: Evaluation of dynamic properties of sands by resonant column testing. Geotech. Test. J. **7**(2), 60–69 (1984)
43. Towhata, I.: Geotechnical Earthquake Engineering 2008; Springer Series in Geomechanics and Geoengineering. Springer, Berlin (2008)
44. Towhata, I.; Haga, K.; Nakamura, S.: Effects of cyclic drained shear or rigidity of sand. In: Proceedings of 20th National Conference on Soil Mechanics and Foundation Engineering 1985, Vol. 1, pp. 591–592
45. Finn, W.D.; Pickering, D.J.; Bransby, P.L.: Sand liquefaction in triaxial and simple shear tests. J. Soil Mech. Found. Div. **97**(4), 639–659 (1971)
46. Seed HB.; Idriss IM.: Simplified procedure for evaluating soil liquefaction potential. J. Soil Mech. Found. Div. **97**(9), 1249–1273 (1971)
47. Rouholamin, M.; Bhattacharya, S.; Orense, R.P.: Effect of initial relative density on the post-liquefaction behaviour of sand. Soil Dyn. Earthq. Eng. **97**, 25–36 (2017)
48. Mazzoni, S.; McKenna, F., Fenves, G.L.: Open System for Earthquake Engineering Simulation (OpenSees) user manual 2006, Pacific Earthquake Engineering Research Center, University of California, Berkeley (http://opensees.berkeley.edu/)
49. McKenna, F.; Scott, M.; Fenves, G.: Nonlinear finite-element analysis software architecture using object composition. J. Comput. Civil Eng. **24**(1), 95–107 (2010)
50. Cui, C.; Jiang, H.; Li, Y.H.: Semi-analytical method for calculating vibration characteristics of variable cross-section beam. J. Vibr. Shock **31**(14), 85–88 (2012)
51. Wang, P.; Zhao, M.; Du, X.; Liu, J.; Xu, C.: Wind, wave and earthquake responses of offshore wind turbine on monopile foundation in clay. Soil Dyn. Earthq. Eng. **113**, 47–57 (2018)
52. Boulanger, R.W.; Curras, C.J.; Kutter, B.L.; Wilson, D.W.; Abghari, A.: Seismic soil-pile-structure interaction experiments and analyses. J. Geotech. Geoenviron. Eng. **125**(9), 750–759 (1999)

53. Arany, L.; Bhattacharya, S.; Macdonald, J.; Hogan, S.J.: Simplified critical mudline bending moment spectra of offshore wind turbine support structures. Wind Energy **18**(12), 2171–2197 (2014)
54. Hu W.-H., Thöns S., Said S., Rücker W.: Resonance phenomenon in a wind turbine system under operational conditions. In: Cunha, E., Caetano, P., Ribeiro, G. Müller (eds.), Proceedings of the 9th International Conference on Structural Dynamics, EURODYN 2014, Porto, Portugal, 2014, A. ISSN: 2311-9020; ISBN: 978-972-752-165-4
55. Jonkman, J.; Butterfield, S.; Musial, W.; Scott, G.: Definition of a 5-MW reference wind turbine for offshore system development. National Renewable Energy Lab (NREL), Golden, CO, United States (2009)
56. Gilbert, R.; Stokoe, K.; Huang, Y.; Munson, J.; Bauer, J.; Hosseini, R.; Hussien, A.: Laboratory testing of lateral load response for monopiles in sand. 2018; BSEE/BOEM TAP, 769